Estimating the 3D shape of volcanic ash to better understand sedimentation processes and improve atmospheric dispersion modelling

Jennifer Saxby[a,*], Alison Rust[a], Frances Beckett[b], Katharine Cashman[a], Hannah Rodger[a]

[a]*Dept. Earth Sciences, Wills Memorial Building, University of Bristol, Queen's Road, Bristol, BS8 1RJ, UK*
[b]*Met Office, FitzRoy Road, Exeter, EX1 3PB, UK*

Abstract

The sedimentation rate of volcanic ash through the atmosphere influences its travel distance, with important implications for aviation and health. The fall velocity of a particle depends on its size and density, but also shape, and volcanic ash is not spherical. To capture the sedimentation of ash, atmospheric dispersion models use empirical drag equations calibrated using geometric shape descriptors. However, particle shape data are scarce and there is no standard method of shape measurement. In addition, shape measurements are not always available during an eruption, when dispersion models are used operationally to forecast ash hazard. We assess the variability in the shape of volcanic ash from Icelandic eruptions using X-ray computed tomography. To consider how good different drag equations and shape descriptors are at representing the sedimentation of volcanic ash we compare calculated fall velocities to measured fall velocities of volcanic ash in air in a settling column. We then suggest the best drag equations and shape descriptors for use in atmospheric dispersion models. We find that shape-dependent drag equations produce more accurate results than a spherical approximation. However, accurate drag calculations based on the shape descriptor sphericity, which is a function of surface area, require the imaging resolution to be within the range of 10^2 - 10^5 voxels per particle as surface area is sensitive to imaging resolution. We suggest that the large-scale form of the particle impacts sedimentation more than small-scale surface roughness. Shape descriptors based on ratios between principal axis lengths are more practical as they are less variable among particle size classes and much less sensitive to imaging resolution. Finally, we use particle shape data from this study and literature sources to make recommendations on default values for use with atmospheric dispersion models where no shape data are available.

Keywords: tephra, atmospheric dispersion, sedimentation, morphology, X-ray tomography

Acknowledgements: This work was supported by the Natural Environment Research Council and the Met Office, UK, as well as the AXA Research Fund and a Royal Society Wolfson Merit Award (to K. Cashman). We thank Sigurður Reynir Gíslason for the Vedde ash sample, Frances Boreham for her assistance in the field while collecting the other samples used in this study, and Tom Davies for his help with tomography data. We thank Claire Witham for her feedback on an earlier draft. We are grateful for detailed reviews provided by Alexa Van Eaton and an anonymous reviewer, which have greatly improved this manuscript.

*Corresponding author
Email address: jennifer.saxby@bristol.ac.uk (Jennifer Saxby)

1. Introduction

Volcanic ash (tephra particles with diameters < 2 mm) can remain in the atmosphere from minutes to days or longer after a large explosive eruption (Durant et al., 2010); the rate of removal from the atmosphere depends on meteorological processes and particle terminal fall velocity. Accurate calculation of terminal velocity requires a parameterisation of particle shape (e.g., Riley et al., 2003; Bagheri and Bonadonna, 2016a,b). This means that forecasts of the movement of volcanic ash clouds generated using atmospheric dispersion models can be sensitive to the shape parameter used in the model's sedimentation scheme (Scollo et al., 2008; Beckett et al., 2015; Saxby et al., 2018). For example, Saxby et al. (2018) found that a 100 μm model particle can travel 44% further from source when it is modelled as non-spherical (sphericity = 0.5). The shape of volcanic ash particles can also provide information on componentry (Buckland et al., 2018), eruptive style (Liu et al., 2015, 2017), transport mechanisms (Rose and Chesner, 1987), emplacement conditions (Dufek and Manga, 2008; Buckland et al., 2018), and tephra layer identification (Liu et al., 2016; Dunbar et al., 2017).

The question of how to measure, and model, particle shape is relevant in many other disciplines. Many atmospheric particulates are non-spherical, meaning that shape is an important parameter in understanding the transport of nuclear fallout (Rolph et al., 2014), ice crystals (Westbrook and Sephton, 2017), pollen (Schwendemann et al., 2007), wildfire embers (Anthenien et al., 2006) and desert dust (Chou et al., 2008). The hydrodynamic behaviour of particles settling in water is also a function of shape; this is important, for example, in analysing assemblages of marine species such as foraminifera, which are used to estimate palaeodepth (e.g., Speijer et al., 2008; Jorry et al., 2006). Particle shape also affects the drag of non-spherical particles in streams (Komar and Reimers, 1978) as well as particle sorting during flow (Oakey et al., 2005). Finally, shape affects crystal settling velocities in magma, with implications for magma evolution and rheology (Higgins and Roberge, 2003).

Another consideration relates to the effect of particle shape on grain size measurement. For example, particles passing through a sieve mesh may have one dimension larger than the mesh aperture, and so the results of sieving are dependent on the shape of the particle (Arason et al., 2011); shape also affects the results of particle size distributions calculated from 2D images (Higgins and Roberge, 2003). Particle volume is a shape-independent

measure of size, but volume is not straightforward to measure for irregular particles.

Volcanic eruptions produce a wide variety of particle shapes, which are related to the kinetics of vesiculation and crystallization during magma ascent, and the fragmentation mechanism. Ash types include vesicular pumice clasts, smooth crystals, platy bubble wall shards, needle-like fragments of tube pumice, and the extremely elongate Pele's hairs formed by low viscosity basaltic melt. Describing shape using one or more geometric shape descriptors reduces operator bias and allows comparison between datasets; however, the most useful shape descriptor will depend on the textural variability of the sample and the purpose of the research, meaning there is no 'standard' way to measure shape. In addition, the results strongly depend on measurement parameters, such as imaging resolution (Alfano et al., 2011; Liu et al., 2015; Dioguardi et al., 2017). Most shape descriptors applied to volcanic ash particles can be measured from projections of particle surfaces via 2D image analysis (e.g., Riley et al., 2003). However, recent advances in the use of optical and electron microscopy (Ersoy et al., 2010; Bagheri et al., 2015; Vonlanthen et al., 2015) and X-ray computed tomography (CT; Ersoy et al. (2010); Dioguardi et al. (2017); Mele and Dioguardi (2018)) mean it is now easy to construct high-resolution 3D models of volcanic ash particle surfaces. We limit our analysis to 3D shape measures, by which most drag equations are calibrated (e.g., Wilson and Huang, 1979; Ganser, 1993; Bagheri and Bonadonna, 2016b; Dioguardi et al., 2017, 2018).

We assess the shape range of volcanic ash and determine how best to measure shape for the purpose of calculating its terminal velocity in an atmospheric dispersion model. We measure multiple 3D geometric shape descriptors using the X-ray CT method. To assess the effectiveness of the shape descriptors in anticipating particle fall velocity, we also measure the terminal velocity of selected mm-sized tephra particles in a settling column and compare the results to calculated terminal velocities using empirical drag equations with our measured shape parameters. From this we provide guidance on the best theoretical approach (drag equation and shape descriptor) for use in atmospheric dispersion models to represent the sedimentation of volcanic ash particles.

Our reference datasets include ash samples from Icelandic volcanoes (Katla, Hekla and Eyjafjallajökull) spanning a wide range of composition, eruptive style, and morphology; this allows us to assess the variation in the shape of volcanic ash between eruptions and between size fractions, and the sensitivity of 3D shape descriptors to the CT scan parame-

ters. We use the resulting insights to present a database of shape descriptors for use with semi-empirical drag equations (Ganser, 1993; Bagheri and Bonadonna, 2016b; Dioguardi et al., 2018) which are valid for a wide range of flow conditions and therefore suitable for modelling the sedimentation of volcanic ash in the atmosphere.

2. Modelling the terminal velocity of non-spherical ash

Particle terminal velocity is defined as the velocity reached by a falling object when the drag force is equal to the gravitational force and acceleration is zero. Volcanic ash particles reach terminal velocity in the atmosphere over distances which are small compared to the distance required to sediment from a plume, and so it is reasonable to neglect acceleration in modelling. Terminal velocity w_t can be calculated as a function of drag:

$$w_t = \left(\frac{4}{3} \frac{d}{C_D} g \frac{\rho_P - \rho}{\rho} \right)^{\frac{1}{2}} \quad (1)$$

where d is the particle size (for a sphere, diameter), g is gravitational acceleration, ρ is fluid density, ρ_P is particle density, and C_D is the drag coefficient, a dimensionless coefficient which is a function of particle shape and flow regime. Volcanic ash falling in air can be subject to several flow regimes, defined by the dimensionless Reynolds number Re; the flow around a particle is classed as laminar when $Re < 0.1$ and turbulent at $Re > 1000$. The drag of spheres can be calculated analytically with high accuracy for all flow regimes (e.g., White, 1974). Solutions for non-spherical particles, which are characterised by higher C_D than spheres of equivalent size and density, are generally empirical or semi-empirical correlations which relate C_D to one or more geometric shape descriptors. Therefore, such correlations are valid for finite Re and limited to particle shape ranges which are covered by the experimental conditions and the formulation used. The complexity in modelling volcanic ash shape means that many operational atmospheric dispersion model setups use a spherical approximation by default (Hort, 2016). In addition, shape data are not always available during an eruption for forecasting purposes.

A spherical particle approximation can be sufficiently accurate for dispersion modelling purposes for small (less than $\sim$ 30 µm diameter) volcanic ash particles in the laminar regime (Alfano et al., 2011; Saxby et al., 2018), but shape begins to strongly influence particle sedimentation and transport distance at particle diameters between $\sim$ 30 and 100 µm, with particles $\geq$ 100 µm being highly sensitive to shape (Beckett et al., 2015; Saxby et al., 2018, in press). There is therefore a need to determine which correlations produce accurate predictions of terminal fall velocity, and are valid for an Re range appropriate for ash dispersion applications, and to provide a database of default shape descriptors, from volcanic ash measurements, for use when no data are available.

3. Tephra samples

We use tephra samples from fall deposits of three Icelandic volcanoes, spanning five eruptions, and collected between 10 and 242 km from vent, to investigate a range of clast types, morphologies, and compositions. Sample locations, compositions and qualitative morphological descriptions are given in Table 1; example ash morphologies are shown in Figure 1. Two samples, KSM and KSU, are noted for their distinctive 'needles' (Figure 1b-d), elongated tube pumice fragments containing sparse microlites and numerous elongated bubbles in a glassy matrix (Larsen et al., 2001). The KVE sample is characterised by numerous flat, platy bubble wall shards (Mangerud et al., 1984). We also examine two more typical examples of Icelandic ash: the EYJ sample is characterised by blocky or angular glassy particles with a wide range of vesicularities (Gislason et al., 2011); the HEK sample is characterised by blocky vesicular particles.

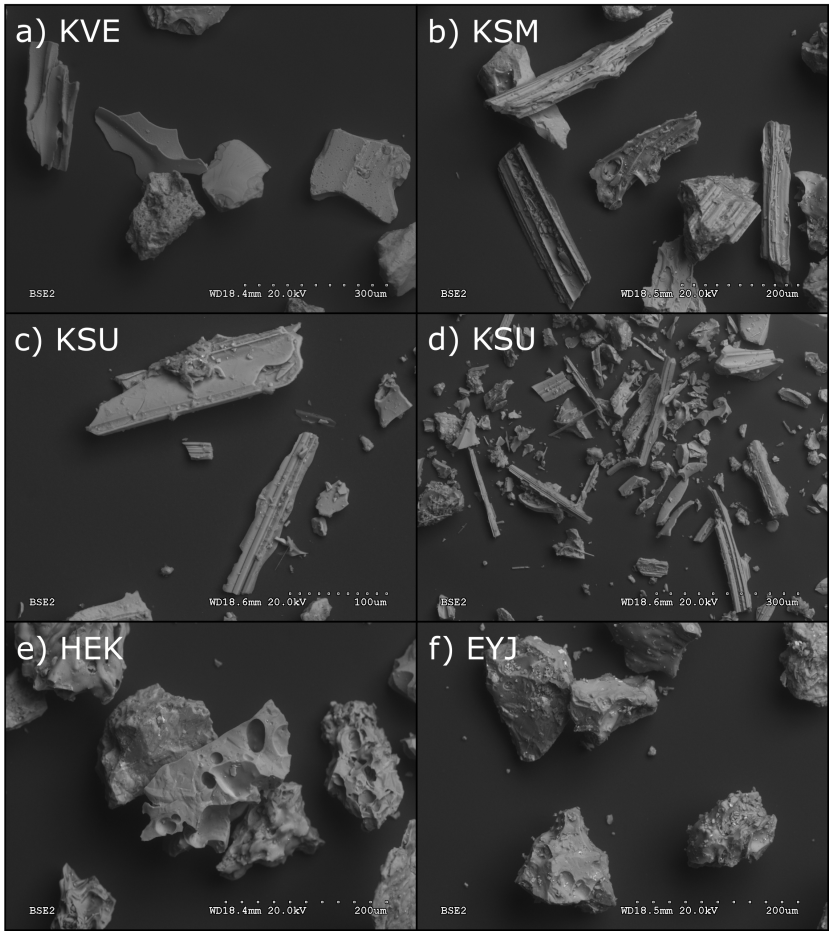

Figure 1: Images showing characteristic morphological characteristics of volcanic ash samples: a) KVE, b) KSM, c-d) KSU, e) HEK and f) EYJ. Images were taken at the University of Bristol using a Hitachi S-3500N scanning electron microscope (SEM). We obtained backscattered electron (BSE) images of particles in the 62.5 – 125 µm sieve fractions (88 – 125 µm for sample KVE).

4. Measurements

Prior to analysis, all samples were manually dry sieved at 1 or 0.5 φ intervals (where φ is a measure of grain size defined as $-log_2 \frac{D}{D_0}$, where D is the diameter of the particle in millimetres and D_0 is a reference diameter of 1mm). We used sieve mesh diameters of 4 to -1 φ (62.5 to 2000 µm), apart from sample KVE which was sieved at half-φ intervals using sieve mesh diameters of 3.5 to -0.5 φ (88 to 1414 µm).

We measured the shape of 19557 particles from KVE, KSU, and HEK using X-ray CT to provide a large volcanic ash shape database, including shape distributions for each sieve fraction, as shape can vary with size (e.g., Mele and Dioguardi, 2018). For this analysis the samples were analysed in bulk, including crystals and lithics. We chose only three samples for this analysis due to the significant scan time needed; the samples we chose span a range of qualitative shape characteristics (see Table 1).

To determine the effectiveness of our measured shape descriptors when used to calculate terminal fall velocity, we also selected 46 individual particles of juvenile glass from the 0 φ and -0.5 φ sieve fractions of the KSM, KVE, HEK and EYJ samples, which were individually scanned using X-ray CT. Particles chosen ranged from 1.0 – 2.6 mm, sufficiently large to image and track; again grains were selected to include a wide range of shapes. As density is a crucial input in drag equations, we also measured the density of these particles. We then considered how well we could calculate the fall velocity of our particles using our shape measurements and different drag equations by comparing to measurements of the fall velocity of the particles in a settling column. KSU particles were not used in this analysis due to their fragility and the greater availability of mm-sized elongate particles in the analogous KSM sample. The following sections give a detailed description of each measurement method.

4.1. Particle velocities

Particle velocities were measured in air using a settling column and high-speed imaging based on the method of Bagheri and Bonadonna (2016b). The 1.5 m high and 0.15 m diameter glass settling column ensures that particles fall a great enough distance to reach terminal velocity. At the top of the column is a guiding tube to ensure particles fall approximately in the centre to minimise errors associated with the particle's position in the

Table 1: Summary of samples used in this study.

Sample ID	Eruption	Year	Composition	Sample location (decimal degrees WGS84)	Notable qualitative shape characteristics
KSM	Katla SILK-MN	2975±12 a BP (Larsen et al., 2001)	Dacitic (∼ 65% SiO_2) (Larsen et al., 2001)	63.49203 -18.880946	Distinctive elongated 'needles'
KSU	Katla SILK-UN	2660±50 a BP (Larsen et al., 2001)	Dacitic (∼ 64% SiO_2) (Larsen et al., 2001)	63.754977 -18.49149	Distinctive elongated 'needles'
KVE	Katla Vedde	∼ 12 ka BP (Wastegård et al., 1998)	Bimodal (45-58% and 72-76% SiO_2 (Mangerud et al., 1984)	65.749955 -17.897997	Flat, platy glass shards
HEK	Hekla 1947	1947	Andesitic (∼ 62% SiO_2) (Larsen et al., 1999)	63.7149 -19.8311	Blocky, vesicular
EYJ	Eyjafjallajökull 2010	2010	Andesitic (∼ 58% SiO_2) (Gislason et al., 2011)	63.7139 -19.725	Blocky or angular glassy particles

column; the setup is illustrated in Figure 2. A Vision Research Phantom v9.1 high speed camera was positioned 0.1 m from the bottom of the apparatus, where particles fell from the settling column into a flat-sided glass box. A measure with precision of 1 mm was placed at the back of the box. To focus the camera prior to the experiments, a weighted thread was lowered down the guiding tube into this box, which was illuminated with two LED lamps. Each grain of ash was then released individually into the guiding tube and filmed at a sample rate of 1400 fps and an exposure of 711.25 µs. Phantom 675.2 Camera Control software was used to output individual video frames in jpeg format, including a time stamp from which terminal velocity could be calculated from 5 to 8 cm sections of each particle's trajectory. The error arising from the relative positioning of the camera, particle, and ruler was corrected assuming that each particle was falling in the centre of the 15 cm main settling column. Each particle velocity measurement presented here represents the median of 5 repeat measurements. Repeat data could not be collected for particles which broke upon landing and so those experiments are not reported; the data we report are for a total of 46 particles which did not break. This creates a potential bias against measuring the fall velocity of particles with certain shapes and densities. Velocity data are available in Supplementary Material.

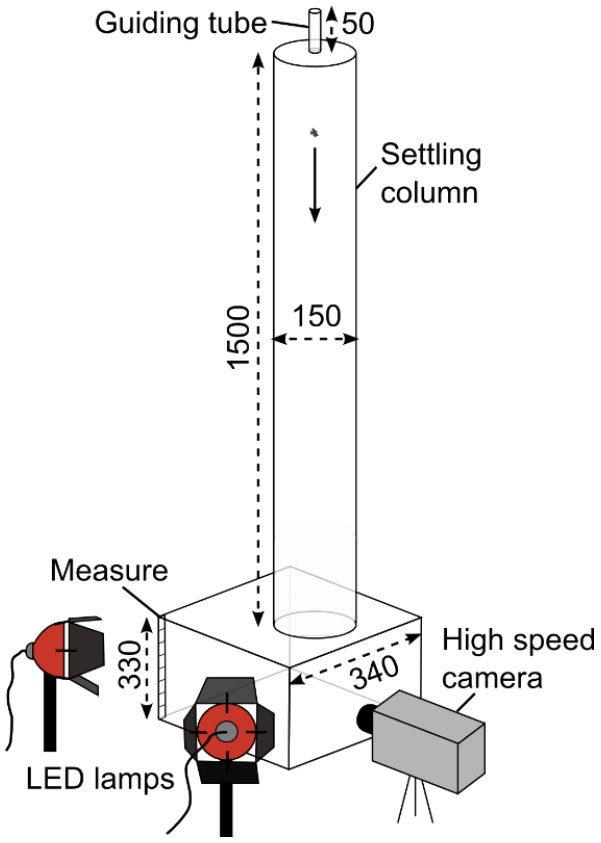

Figure 2: Schematic diagram of the settling column setup to measure terminal velocity in air. All dimensions are in mm.

4.2. Density

We calculated particle density using volumes from X-ray CT scans and particle mass measured on a balance with a precision of 0.0001 g. Particle dimensions calculated using Avizo CT software were checked using digital calipers, to ensure that CT data gave accurate particle size measurements. Density data are available in Supplementary Material.

4.3. Particle dimensions using X-ray CT

All particle scans were carried out on a Nikon XTH225ST scanner using a voltage of 120 kV and a current of 58 µA. The 46 particles for which we obtained terminal velocity measurements were individually scanned by mounting in florist's foam or cotton wool within plastic pipettes. Of these, 16 were scanned at the maximum instrument resolution (voxel edge length = 3 µm, where a voxel is a volumetric (3D) pixel). We obtained this high-resolution dataset as shape descriptors can be sensitive to imaging resolution (Liu et al., 2015); to determine the sensitivity of shape descriptors to resolution we progres-

sively resampled the data to give resolutions of 2, 4, 8, 16 and 32 times the original voxel edge lengths. The remaining 30 particles were scanned at the lower resolution of voxel edge length = 96 µm (32 times the voxel edge length of the high-resolution scans).

For bulk scanning of the KVE, KSU and HEK samples, we used a voltage of 100 kV and a current of 70 µA. We measured all sieve fractions of these samples (62.5 to 2000 µm for KSU and HEK, 88 to 1414 µm for KVE). The voxel size was varied to maintain a minimum resolution of between 4728 and 20,000 voxels per particle, to obtain size-independent shape parameters; within this range we find no correlation between resolution and shape. Samples were encased in epoxy resin to ensure good particle separation and allow simultaneous imaging of up to several hundred particles, as discussed in Saxby et al. (2018). Despite this preparation, particles from coarser sieve fractions tended to float to the top of the sample container before the epoxy hardened; these particles were touching in the resulting segmented 3D volumes and were separated using a watershed algorithm (Avizo Separate Objects module), which first detects object centres and then simulates flooding from these regions to the edges of 3D 'catchments' defined according to the greyscale value gradient.

For all scans, we reconstructed 3D volumes using CT Pro 3D software and segmented the volumes in Avizo. From the resulting particle surfaces, we obtained particle surface area (A_{surf}), volume (V), and three orthogonal principal axis lengths: long axis L, intermediate axis I and short axis S.

It is important to note that benchtop X-ray CT cannot be used to accurately quantify the shape of the finest volcanic ash fractions relevant to aircraft hazard ($<$ 30 to 60 µm; Rose and Durant (2009) or respiratory health ($<$ 4 to 10 µm; Horwell et al. (2010)), due to constraints on imaging resolution. Although synchrotron X-ray CT systems can achieve resolutions of 1 µm or less, in our system the minimum voxel edge length is $\sim$ 3 µm. For this reason, particles smaller than 62.5 µm (4 φ) were not used, and our X-ray CT analysis does not give a full grain shape distribution for the range of sizes typically used to initiate operational dispersion models ($\sim$ 0.1 – 100 µm; Hort (2016)). However, the terminal velocity of very small particles ($< \sim$ 30 µm) is low compared to atmospheric turbulence and vertical advection (Saxby et al., 2018), meaning that the dispersion of these particles (Class III fragments in the classification of Koyaguchi and Ohno (2001)) is less sensitive to shape. For example, for model particles of 1 µm, diffusion to ground level from

12 km above ground level is faster than sedimentation over the same distance (Saxby et al., 2018). Therefore we suggest it is reasonable to apply the same shape factors for particles smaller than $\sim$ 30 μm despite the lack of available measurements. However, we note that drag may be important for particles $< \sim$ 30 μm as it affects the two-way coupling of fine ash and turbulent eddies (Del Bello et al., 2017).

4.4. Morphological parameters

We compared observed terminal fall velocities with calculations based on the drag equations of Ganser (1993), Bagheri and Bonadonna (2016b) and Dioguardi et al. (2018); to calculate drag by these equations, we measured the shape descriptors used in their design. The drag equations are all applicable for the range of flow regimes expected for volcanic ash falling in air and are all calibrated using 3D geometric shape descriptors. We calculate w_t using equation 1; all the drag equations use the diameter of a volume-equivalent sphere, d_v, for the particle size parameter d. C_D is calculated as a function of one or more geometric shape descriptors, given below; for the corresponding C_D equations, see Supplementary Material. Since the drag of spheres can be determined analytically to high accuracy, a popular approach in defining shape descriptors is to use a ratio of a particle parameter to that of a volume-equivalent sphere. The Ganser (1993) drag equation uses sphericity ψ_G, the ratio of surface area of a volume-equivalent sphere to surface area of the particle being described:

$$\psi_G = \frac{\pi^{\frac{1}{3}} (6V)^{\frac{2}{3}}}{A_{\text{surf}}}, \tag{2}$$

where A_{surf} is a measure of 3D surface area and therefore an effective descriptor of roughness scales limited only by imaging resolution. Difficulty in measuring the 3D surface area of irregular particles has meant that studies have often calculated sphericity using approximate surface area of a smooth scalene ellipsoid A_e (Dellino et al., 2005; Mele et al., 2011), with equal principal axes to the particle:

$$A_e = 4\pi \left(\frac{\left(\frac{L}{2}\right)^z \left(\frac{I}{2}\right)^z + \left(\frac{L}{2}\right)^z \left(\frac{S}{2}\right)^z + \left(\frac{I}{2}\right)^z \left(\frac{S}{2}\right)^z}{3} \right)^{\frac{1}{z}}, \tag{3}$$

where $z = 1.6075$. The Dioguardi et al. (2018) drag equation is calibrated using an ellipsoid approximation; their shape descriptor Ψ_D, which we term the Dioguardi shape factor, is the

ratio of 3D sphericity to 2D circularity:

$$\Psi_D = \psi_e / X \tag{4}$$

(Dellino et al., 2005; Dioguardi et al., 2018), where:

$$\psi_e = \frac{\pi^{\frac{1}{3}} (6V)^{\frac{2}{3}}}{A_e} \tag{5}$$

and

$$X = \frac{P_{\text{proj}}}{P_c}; \tag{6}$$

P_{proj} = maximum projected perimeter and P_c = the perimeter of a circle with equal projected area to the particle being described. In this study we focus on 3D shape measurement and do not measure X, as this 2D parameter is a function of particle perimeter, one of the 2D parameters most sensitive to imaging resolution (Liu et al., 2015). When calculating the Dioguardi shape factor we use the Dioguardi et al. (2018) best fit approximation:

$$\Psi_D \approx 0.83 \psi_e. \tag{7}$$

Another class of particle shape descriptor, termed form factors, combines L, I and S, which measure the form of the particle but are insensitive to small-scale surface roughness (Bagheri and Bonadonna, 2016b) and are therefore less sensitive to imaging resolution. These include the two shape factors defined by Bagheri and Bonadonna (2016b), elongation e and flatness f, where

$$e = \frac{I}{L} \tag{8}$$

and

$$f = \frac{S}{I}. \tag{9}$$

The shape descriptors we measure (sphericity, the Dioguardi shape factor, elongation and flatness) are all scaled between 0 and 1, where 1 = an equant particle; this allows for easy comparison between parameters.

5. Results

5.1. Sensitivity of shape descriptors to CT scan and reconstruction parameters

5.1.1. Greyscale threshold

Particle surfaces are reconstructed from raw CT data by separating 3D regions representing particles from the surrounding epoxy; this requires the selection of a threshold greyscale value. As the particle edges are characterised by a gradient (over $\sim 3 - 5$ voxels) rather than a sharp boundary, the choice of threshold is subjective and so we determined the sensitivity of particle volume and shape to this choice. We did this by increasing and decreasing our best estimate greyscale threshold by 10, which covered the particle boundary gradients; the results and example greyscale images are given in Supplementary Figure A1. We calculate a maximum 6% error on mean d_v and 4% error on mean sphericity arising from the selection of the particle boundaries.

5.1.2. Voxel size

As shape can be sensitive to imaging resolution, we investigated the impact of voxel size on measured shape factors using X-ray CT data for 16 individual particles. Scans were conducted at the scanner's maximum resolution (a voxel edge length of ~ 3 µm, giving between 6.5×10^6 and 1.3×10^8 voxels per particle). We progressively resampled the scan data from 2 to 32 times the original voxel edge lengths, giving a maximum voxel edge length of ~ 96 µm; after each resampling we recalculated surface area, volume, sphericity, the Dioguardi shape factor, elongation, and flatness.

The results are shown in Figure 3 and highlight the sensitivity of surface area, and the surface area-based shape factor sphericity, to resolution. For a large, rough particle (KSM-9, Figure 3, inset), apparent surface area decreased by between 10 and 23% each time we doubled the voxel edge length; the mean surface area decrease for all particles at all scales is 12%. In contrast, volume measurements are relatively insensitive to imaging resolution: when halving or doubling the resolution, the mean absolute volume change is 1.4%. This means the particle diameter d_v is insensitive to resolution over this range. The shape descriptors vary in their sensitivity to resolution. Particles have higher apparent sphericity at low resolution: doubling the voxel edge length resulted in sphericity increasing between 0.005 and 0.13 (3 – 32%, mean 14%). For most particles studied, sphericity and surface area are sensitive to resolution for the whole resolution range, suggesting the particles ex-

hibit surface irregularities below the scale of the 3 µm resolution limit. The exceptions are the Vedde ash particles KVE-1 and KVE-2, which are smooth glass shards (Figure 3, insets). For these particles, surface area and sphericity are almost constant above $\sim 10^5$ voxels / particle. Unlike sphericity, shape descriptors which are functions of principal axis lengths (the Dioguardi shape factor, elongation, and flatness) are relatively insensitive to imaging resolution (Figure 3 d-f), and change on average by ± 1.2%, 1.6%, and 1.3% respectively when voxel edge length is doubled.

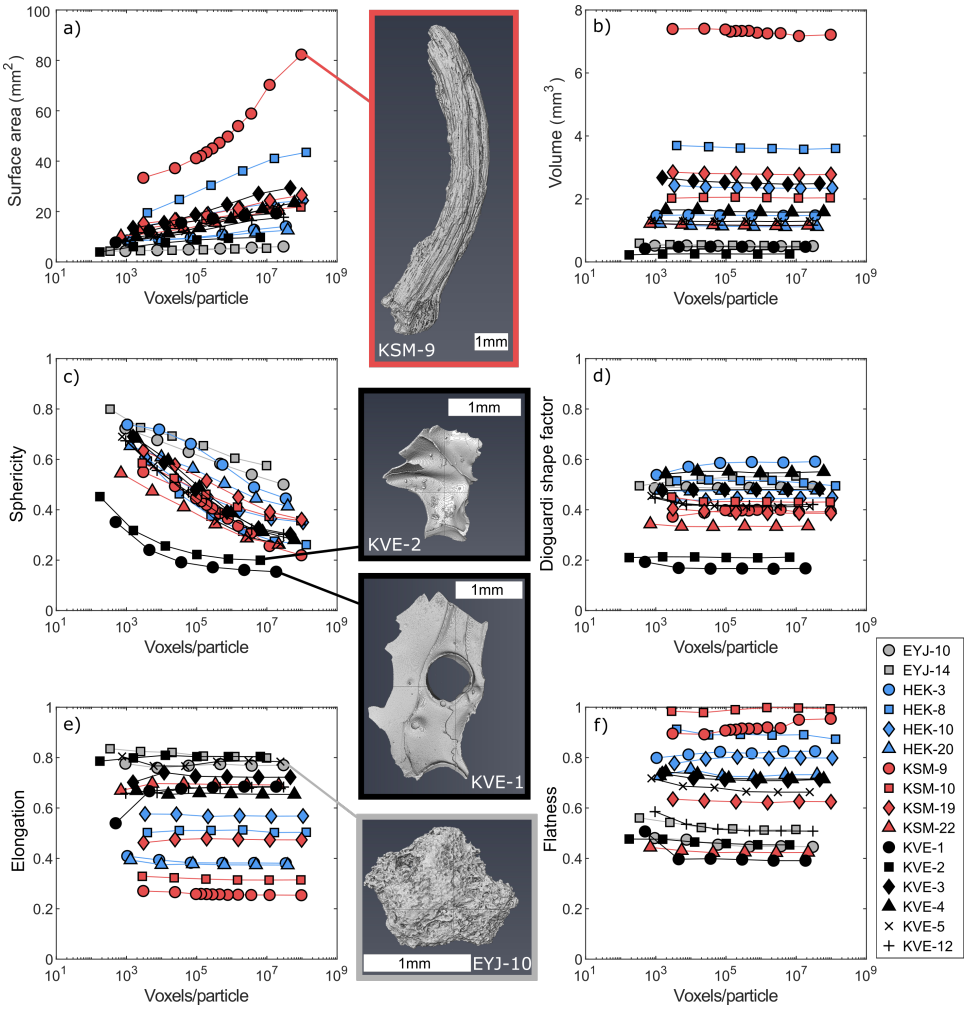

Figure 3: Sensitivity of particle measurements to CT imaging resolution. a) Surface area A_{surf}; b) volume V; c) sphericity sphericity (Ganser, 1993); d) shape factor the Dioguardi shape factor (Dioguardi et al., 2018); e) elongation elongation (Bagheri and Bonadonna, 2016b); f) flatness flatness (Bagheri and Bonadonna, 2016b).

5.2. *Assessing the effectiveness of shape descriptors in representing the aerodynamic behaviour of volcanic ash*

Recorded median terminal velocities ($w_{t,\ rec}$) of particles dropped in the settling column range from 1.9 to 6.4 m s^{-1}. Minimum and maximum velocities deviate from the median by $\leq 57\%$. We compare measured fall velocity to calculated fall velocities using shape-based drag equations (Ganser, 1993; Bagheri and Bonadonna, 2016b; Dioguardi et al., 2018) with our measured shape parameters, as well as a spherical particle drag equation (White, 1974). We calculate terminal velocity as a function of the drag coefficient defined by these equations; where a shape factor is required we use our X-ray CT measurements. The full drag equations are given in Supplementary Material.

5.2.1. *Effect of scan resolution on velocity calculations using sphericity*

For the Ganser (1993) drag equation, which uses the shape factor sphericity that is very sensitive to imaging resolution, we first recalculate terminal velocity using every value of sphericity obtained from resampling the CT data for the 16 high resolution scans (Figure 3c). A mean 14% reduction in sphericity for each doubling of voxel edge length translates into an average reduction of 12% in calculated velocity ($w_{t,\ Ganser}$). Figure 4 shows these calculated velocities relative to $w_{t,\ rec}$. Importantly, we find that calculating sphericity with high-resolution data results in velocity underestimation, as we overestimate the effect of very small-scale surface irregularities on drag. For example, using the original (high resolution) scan settings to calculate surface area predicts fall velocities ($w_{t,Ganser}$) that are 1.2 – 2.3 times too slow. The best agreement between measured velocities and those calculated using the Ganser scheme occurs when we calculate sphericity using the largest voxel edge length of 96 µm (resolutions between 10^2 and 10^5 voxels / particle). For the comparison of drag equations in the following section, we use this best fit dataset, with sphericity calculated using a resampled 96 µm resolution, for the 16 particles scanned at high resolution, for consistency with the remainder of the 46 particles which were scanned at 96 µm resolution.

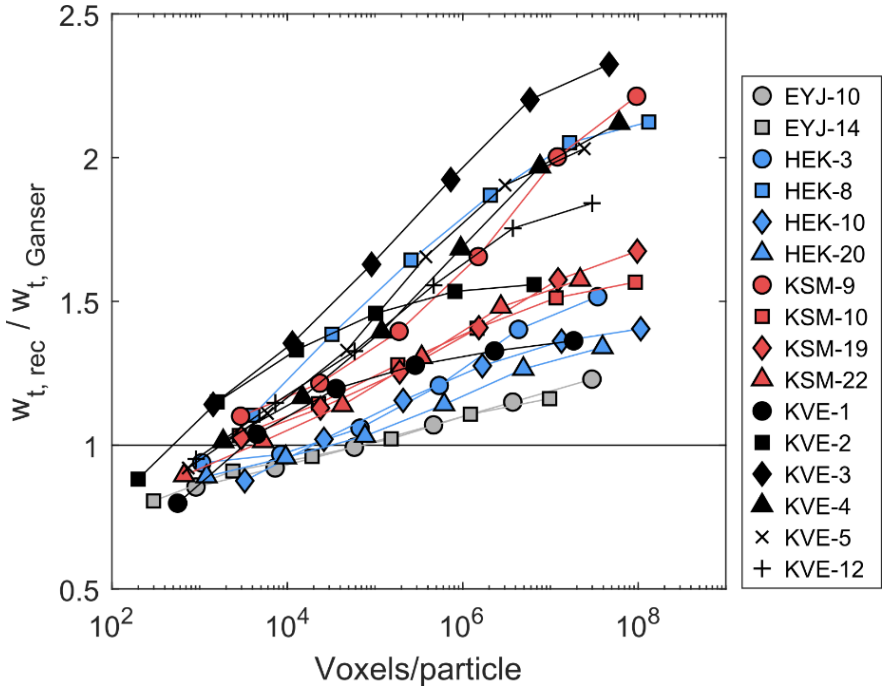

Figure 4: Measured velocity ($w_{t,\,rec}$) divided by velocity calculated after Ganser (1993) ($w_{t,\,Ganser}$) with sphericity calculated after progressive resampling of CT datasets to decrease resolution. Values of 1 indicate perfect agreement between $w_{t,\,rec}$ and $w_{t,\,Ganser}$. Higher scan resolutions result in higher surface area measurements, which give lower sphericity values and therefore calculated velocity which is too low.

5.2.2. *Effectiveness of published drag equations*

The results of our comparison between drag equations are shown in Figure 5. The analytical drag equation of White (1974) for spheres overestimates terminal velocity with a mean absolute percentage error (MAPE) of 40% (Figure 5a); drag equations which include a shape factor (Ganser, 1993; Bagheri and Bonadonna, 2016b; Dioguardi et al., 2018) produce better agreements with measured velocities. The Bagheri and Bonadonna (2016b) scheme calculates velocity as a function of elongation and flatness, which are insensitive to resolution; the scheme slightly overestimates terminal velocity, with a MAPE of 24% (Figure 5c). Velocity calculated using the Dioguardi shape factor (equation 7) and calibration (Dioguardi et al., 2018) yields a MAPE of 22% (Figure 5b). Using the Ganser (1993) scheme with sphericity calculated using a voxel edge length of 96 µm results in a MAPE of 19% (Figure 5d). We show only this best fit dataset; using the sphericity data from the high resolution scans with no resampling increases the MAPE of the Ganser (1993) scheme to 69%, meaning the drag equation performs worse than a spherical approximation if the impact of surface roughness is overestimated.

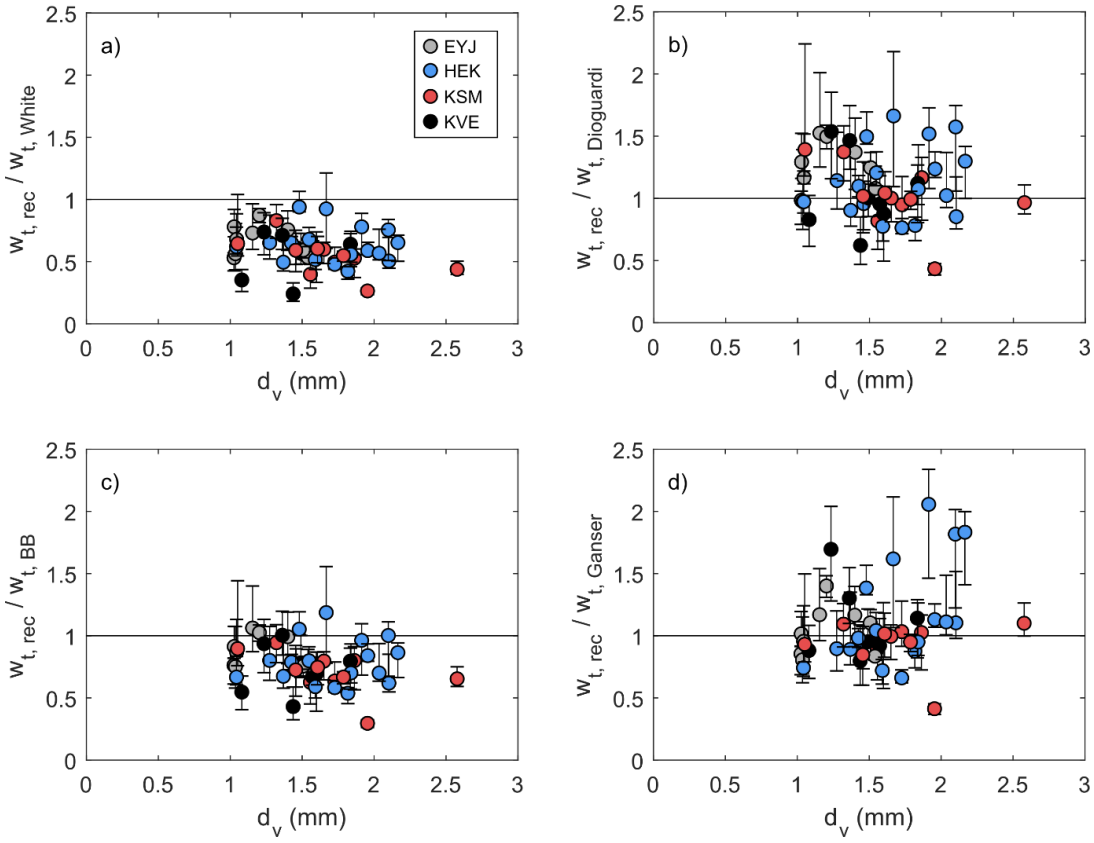

Figure 5: Measured velocity ($w_{t,\,rec}$) divided by velocity calculated by a) a spherical particle approximation (White, 1974), b) as a function of the Dioguardi shape factor (Dioguardi et al., 2018), c) as a function of elongation and flatness (Bagheri and Bonadonna, 2016b), and d) as a function of sphericity (Ganser, 1993) where sphericity is calculated using CT scan resolutions of 96 µm voxel edge length. Note that the Ganser (1993) scheme performs worse than even a spherical particle approximation when sphericity is calculated using much higher image resolutions.

5.3. A database of the shape of volcanic ash

We have determined that the drag equations of Ganser (1993), Bagheri and Bonadonna (2016b), and Dioguardi et al. (2018) all produce reasonable estimates of volcanic ash terminal velocity. In practice, when forecasting ash dispersion operationally, information on particle morphology is unlikely to be available. Therefore, the use of these schemes requires a database from which to choose a default ash shape.

5.3.1. Volcanic ash shape data selection criteria

It is important to assess the relationship between particle shape and size, as well as to obtain shape data for particles smaller than the mm-sized particles we used in settling column experiments. Operationally, Volcanic Ash Advisory Centres use volcanic ash dispersion models with a particle size distribution (PSD); for most operational systems the

bulk of the modelled erupted mass is restricted to particles with diameter < 100 μm (Hort, 2016).

As illustrated above, another important consideration is the resolution used to obtain sphericity (Figure 3). Accurate calculation of terminal velocity using the Ganser (1993) scheme requires sphericity to be calculated from CT data with a resolution which gives between 10^2 and 10^5 voxels / particle, and so our database can only include sphericity data in this resolution range. Because the Dioguardi shape factor, elongation and flatness are not sensitive to imaging resolution, it is possible to directly compare our data to other studies measuring the same shape factors, regardless of experimental conditions. We calculated these shape factors using equations 7, 8, and 9, where only axis lengths or approximate ellipsoid sphericity ψ_e were reported. We also exclude studies which use different shape equations; for example, many studies calculate approximate sphericity using 2D images. We prefer to limit our analysis to the exact shape descriptors by which the drag equations were calibrated.

We obtain shape descriptors for every sieve fraction of samples KVE, KSU, and HEK, adjusting voxel size, with a resolution of 4728 – 20,000 voxels / particle. The resulting particle shape distributions are shown in Figure 6; we compare them in Figure 7 to published data from other eruptions that match our criteria. All particle shape data are available in Supplementary Material.

Our samples, and most of the samples from literature sources in Figure 7, are bulk samples of all components (glass, crystals, lithics) of an eruption; the exception is single-component data from Wilson and Huang (1979) which we show for comparison but exclude from analysis as for dispersion modelling purposes we are interested in all particle types.

5.3.2. New ash shape results

Sphericity changes significantly with particle size for all eruptions in this study (Figure 6). Particles of ~ 300 μm are the least spherical, with the lowest median sphericity of 0.27 and 0.36 respectively for the 250 μm sieve fractions of the HEK and KSU ash, and a lowest median sphericity of 0.17 for the 354 μm sieve fraction of the KVE ash (Figure 6a-c). For all samples, sphericity is highly variable even within a single size fraction. The Dioguardi shape factor (Dioguardi et al., 2018) shows a similar pattern, although with fewer extremely high or low values (and fewer outliers). The lowest median values of the Dioguardi shape factor are 0.34 (HEK, 125 μm), 0.21 (KVE, 354 μm), and 0.34 (KSU, 250 μm) (Figure 6d-

f). Flatness and elongation, in contrast, do not show significant variation with particle size, and both shape factors are constrained to a narrower range, with median elongation and flatness between 0.56 and 0.81 for all samples and size fractions in this study (Figure 6g-l). The KSU sample, chosen for its 'extreme' elongated grain shapes when viewed under an optical microscope, does not differ markedly from HEK, an ash sample which appears more 'typical' on visual inspection, in terms of median values, although the percentage of particles with lower shape factors is higher for the KSU ash. The KSU ash has more elongated particles (24 % of particles have elongation < 0.5) than KVE (9 %) or HEK (6 %). However, the percentage of particles with flatness < 0.5 is low for all samples: 2 % for HEK, 3 % for KVE, and 4 % for KSU.

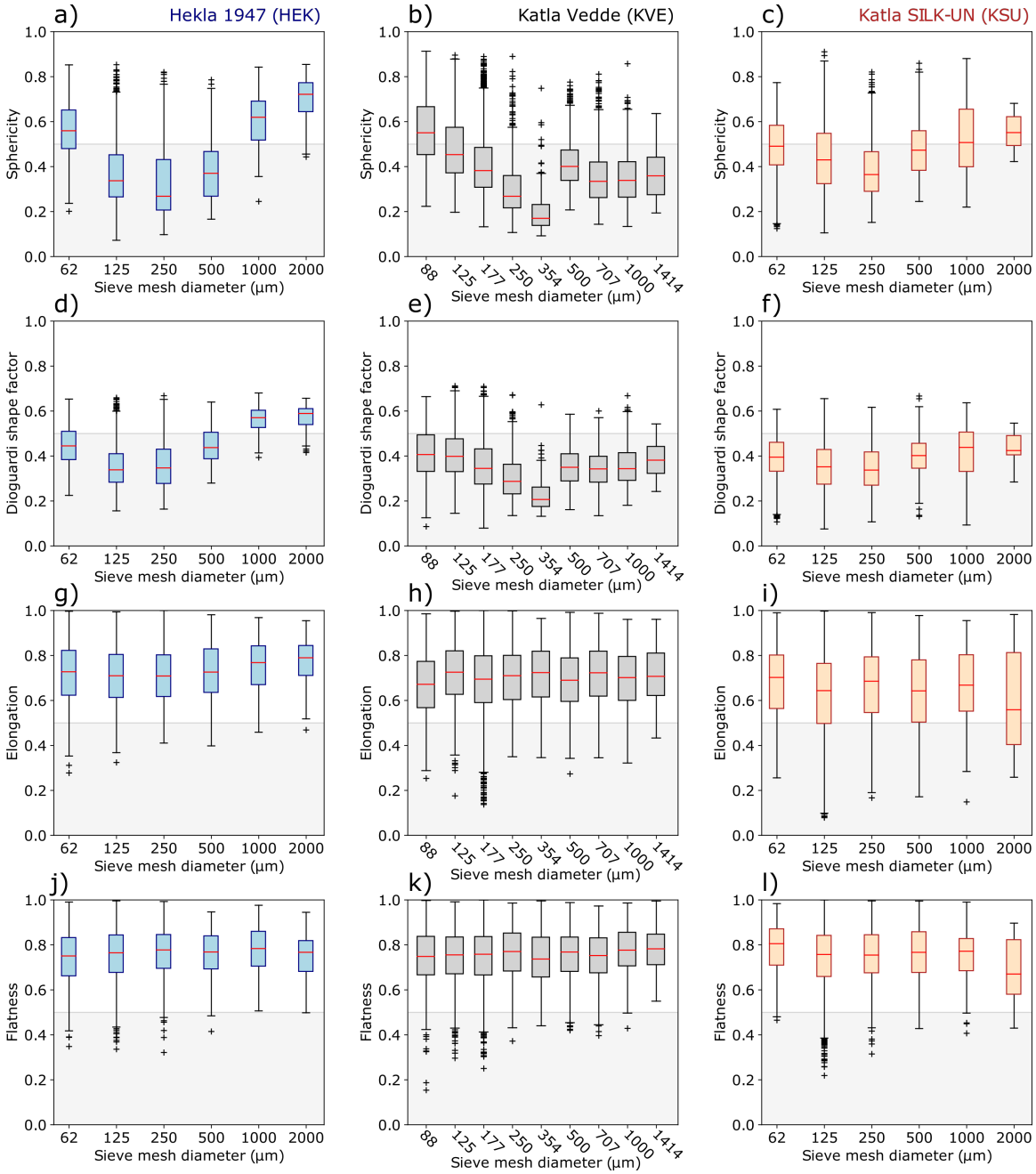

Figure 6: Shape distributions for bulk sieved samples HEK, KVE, and KSU. We chose three samples due to the scan time needed; the samples span a range of qualitative particle shape characteristics (Table 1). We shade each plot to highlight shape factors < 0.5 to aid visual comparison of the proportion of highly non-spherical particles in each sample. Red lines indicate the median; boxes show the interquartile range; crosses indicate outliers.

5.3.3. *Volcanic ash shape database*

We compare our shape data to data from previous studies, to expand our morphology database to include different eruptions and particle size fractions, and to determine whether

the eruptions studied here show a 'typical' range of volcanic ash shape. All ash shape data are given in Figure 7. As data vary between studies, we plot only mean and standard deviation of shape for each sample. Some studies report the mean shape factor for each size fraction of a sample; others give the mean shape of a bulk sample; where the particles vary in size, we indicate the size range using the X-axis error bars. We note that methods of measuring grain size differ between studies, and so the size ranges shown here should be considered approximate. For the shape descriptor sphericity, we include only data from studies that use CT data with a resolution of between 10^2 and 10^5 voxels/particle, which is our recommendation. Despite this limitation we still find a weak correlation between image resolution and sphericity (Figure 7b).

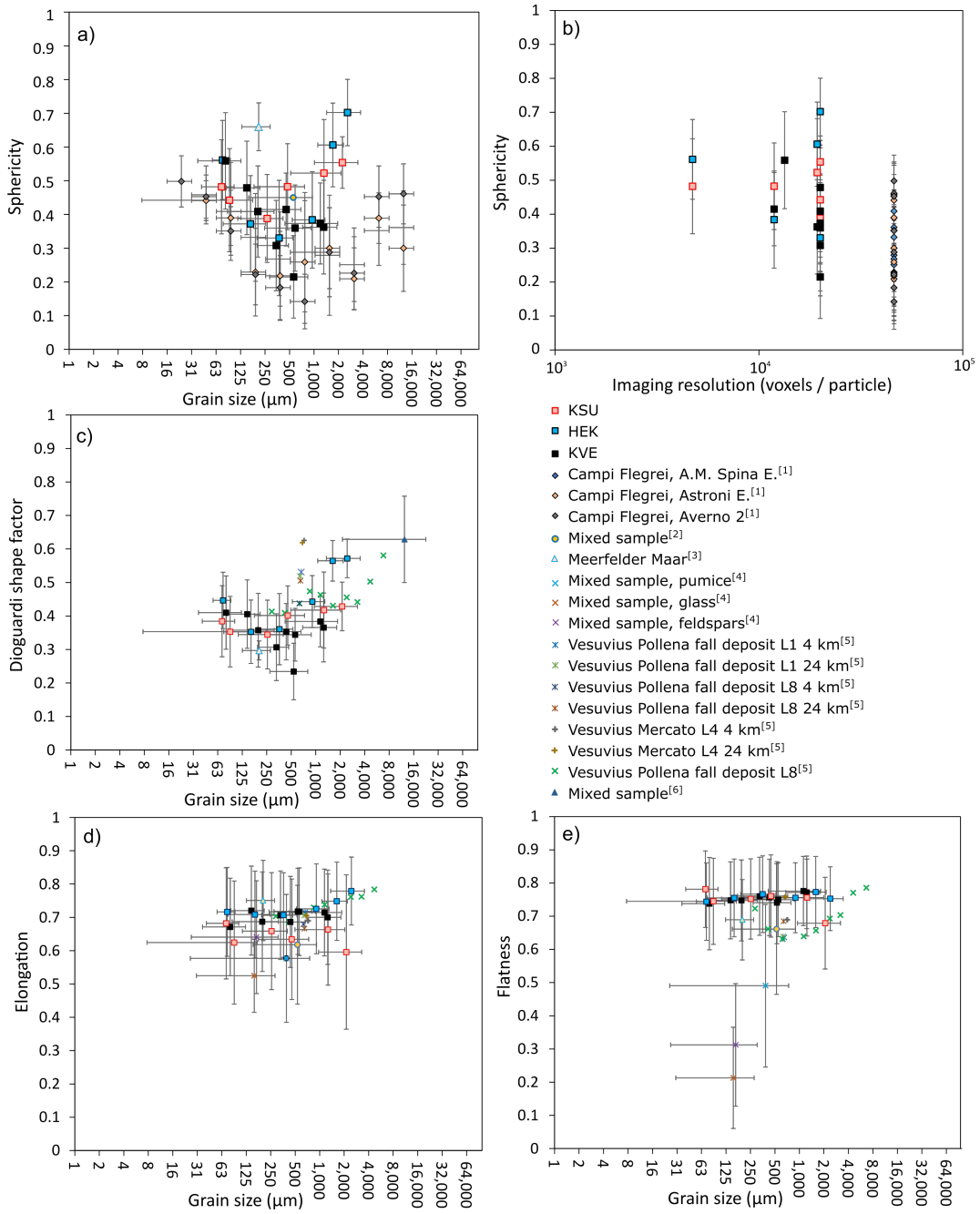

Figure 7: Shape measurements of volcanic ash particles from this study and published literature: a-b) sphericity (Ganser, 1993), c) the Dioguardi shape factor (Dioguardi et al., 2018), d) elongation and e) flatness (Bagheri and Bonadonna, 2016b). X-axis error bars indicate the grain size range, with points plotted at the middle of the range; Y-axis error bars show one standard deviation of shape for each sample, with points indicating mean shape. 'Mixed sample' indicates ash from multiple eruptions; see Supplementary Material for specifics. Data sources: [1]Mele and Dioguardi (2018); [2]Bagheri et al. (2015); [3]Vonlanthen et al. (2015); [4]Wilson and Huang (1979); [5]Mele et al. (2011); [6]Dioguardi et al. (2018). We exclude data from studies which use different shape equations or which calculate sphericity using data outside the range of image resolution we find to be effective.

Figure 7a shows that sphericity ranges from $\sim$ 0.1 to 0.8 for particles between 10^1 and 10^4 μm. Where multiple size fractions of the same sample are measured, the relationship between sphericity and grain size is similar to samples from this study: particles at the extremes of the size range are more spherical, with a pronounced low in sphericity occurring between 125 and 1000 μm. A similar pattern can be observed for the Dioguardi shape factor (Figure 7c). There is less variation in flatness; most samples have flatness between 0.5 and 0.9, using the ranges given by one standard deviation for all samples. The single-component (glass and feldspar) samples of Wilson and Huang (1979) are an exception, with mean flatness between 0.2 and 0.5. Mean elongation for all samples ranges between 0.4 and 0.9. The KSU data are more elongated (lower elongation) than most other data from the literature, as expected from visual inspection of the samples, which contain characteristic tube pumice 'needles'. However, neither the KSU or KVE samples differ greatly from the other ash shape data in any mean shape factor.

6. Discussion

6.1. *Measuring shape*

X-ray CT is an accurate and efficient method of assessing particle size and shape in 3D, and allows imaging of hundreds of particles, and multiple shape factors, relatively rapidly. The analytic error resulting from manual selection of greyscale values is low (< 4 % on sphericity, which is insignificant compared to its sensitivity to image resolution, and < 6 % on diameter d_v). The high resolution makes it an invaluable tool for examining detailed structures in volcanic rocks. For shape quantification, however, high resolution surface area measurements result in very low sphericity and therefore underestimate terminal velocity by the drag equation of Ganser (1993). We recommend using a resolution between 10^2 and 10^5 voxels/particle to calculate sphericity. The best agreement between measured velocity $w_{t,\ rec}$ and calculated velocity $w_{t,\ Ganser}$ is reached at a range of image resolutions; we suggest this is due to the range of particle shapes as well as uncertainty on other parameters such as density, diameter, particle position in the settling column and the variability in velocity resulting from changing orientation (e.g., Saxby et al., 2018). Using shape parameters based on principal axis lengths is a more practical technique where imaging resolution cannot be kept constant. We conclude that above our lower resolution limit of $\sim 10^2$ voxels/particle, imaging resolution is not a concern for calculation of these shape descriptors, meaning that for calculation of elongation, flatness or the Dioguardi shape factor it is practical to sacrifice higher resolution in favour of speed.

As shape parameters based on axis lengths are less sensitive to resolution, we assess the accuracy of the Ganser (1993) drag equation when using the approximate sphericity of a smooth ellipsoid with equivalent axes to the particle (ψ_e; Equation 5) in place of a surface area based formula (Equation 2). The results are shown in Figure 8. Calculated velocities are accurate for the particles in this study, with MAPE of 23%, compared to MAPE of between 19% and 69% depending on image resolution for the surface area formulation. Therefore, it is valid to use the Ganser (1993) drag equation with approximate sphericity ψ_e in place of sphericity for rough particles.

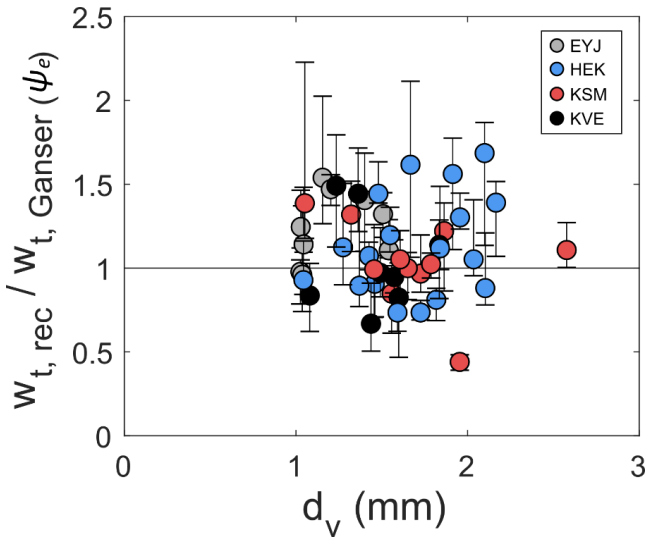

Figure 8: Measured velocity ($w_{t,\ rec}$) divided by velocity calculated according to the drag equation of Ganser (1993) as a function of approximate sphericity ψ_e. Values of 1 indicate perfect agreement between measured and calculated velocity. The mean absolute percentage error is 23%.

6.2. The shape range of volcanic ash

Particle sphericity and the Dioguardi shape factor are size-dependent: in our samples, and others from the published literature, particles of $\sim$ 125 to 1000 µm have the lowest shape factors (i.e. are the most extreme-shaped). Although sphericity is sensitive to image resolution, a similar trend seen in values of the Dioguardi shape factor, which is insensitive to image resolution, suggests that the size dependence is not an artefact of CT scan parameters. Instead, the correlation between size and shape is likely to be linked to bubble size. Although we do not measure bubble size in this study, the size of bubbles influences fragmentation (Liu et al., 2017); modal values of bubble size are typically 100 – 1000 µm (Rust and Cashman, 2011), corresponding to the lowest-sphericity particles. Bubbles, along with crystals, control the surface irregularities of volcanic ash particles, meaning that similarity between the particle size and the bubble size can produce highly irregular particle surfaces. Indeed, a recent X-ray CT study of volcanic ash particles (Mele and Dioguardi, 2018) found that surface irregularity increased as the particle size neared the bubble size; bubble size could similarly be a primary control on shape for our samples. If the 125 to 1000 µm size fraction of a volcanic ash sample included a significant proportion of phenocrysts with higher sphericity than rough vesicular pumice fragments, this could increase bulk sphericity; however the samples in this study do not contain abundant phenocrysts.

Shape factors based on principal axis lengths (elongation and flatness) do not change significantly with particle size or between eruptions (Figures 6 and 7). The exceptions are three samples measured by Wilson and Huang (1979), with mean flatness as low as 0.2, whereas most other data are 0.6 – 0.8 (Figure 7e). This difference may be partly because they separate the ash into components, with the lowest flatness from a sample of purely glass shards, whereas most of the other studies listed use bulk samples. Glass shards form from bubble wall fragments and have a characteristically flat morphology when particle size is similar to the bubble size. We do not include the Wilson and Huang (1979) data when assessing a default range of flatness to use in dispersion modelling; however, we note that some components of a volcanic ash sample can have much more 'extreme' shapes than the bulk.

Some of our samples were chosen for the presence of 'extreme' shaped grains (KSU, KVE); these do in fact contain a higher proportion of particles with shape descriptors < 0.5 (more extreme shapes) than the more 'normal' HEK sample (Figure 6). However, despite the presence of unusually shaped grains, mean shape values do not differ significantly from bulk ash samples in other studies, although they do differ from hand-picked juvenile samples of Wilson and Huang (1979) (Figure 7). This suggests that the range of values we observe for elongation, flatness, sphericity and the Dioguardi shape factor are valid as 'average' values for modelling purposes even for eruptions which produce unusual ash shapes. However, we note that we do not consider the most extreme-shaped pyroclasts such as Pele's hair.

6.3. Using shape in dispersion models

The drag equations of Ganser (1993), Bagheri and Bonadonna (2016b) and Dioguardi et al. (2018) produce reasonable estimates of terminal velocity, which are more accurate than a spherical assumption, for volcanic ash and lapilli particles in the range 1.0 – 2.6 mm. The schemes are all valid for a wide range of flow regimes, and the Ganser (1993) and Bagheri and Bonadonna (2016b) drag equations are accurate for low-Re analogue particles (equivalent to volcanic ash from 1 µm to 1 mm in diameter; Saxby et al. (2018)). All are therefore suitable for use in atmospheric dispersion models used to produce operational forecasts of distal volcanic ash dispersion, which are usually initiated using a range of particle size classes. Of the three drag equations, the one chosen for inclusion in a dispersion model will most likely depend on the shape data available, as they are functions of different

geometric shape descriptors. Although the Ganser (1993) law produces the lowest average error on terminal velocity for our dataset (19%), it requires a specific imaging resolution range for surface area measurement. We consider the Dioguardi et al. (2018) law equally accurate given its similar error (22%). In addition, if we calculate the Dioguardi shape factor using the approximation given in Equation 7, it is solely a function of the three principal axis lengths of a particle and so results are independent of imaging resolution for the range investigated. The Bagheri and Bonadonna (2016b) drag equation produces a similar error (24%) for the data in this study; it uses the shape descriptors elongation and flatness, which vary less between eruptions and size classes than the shape descriptors of Ganser (1993) and Dioguardi et al. (2018). Therefore, we recommend the use of the Bagheri and Bonadonna (2016b) drag equation where it is convenient to assume a constant shape value across all size fractions of the PSD.

For volcanic ash we found that an imaging resolution of 10^2 - 10^5 voxels per particle is required for determining surface-area-dependent shape parameters for accurate drag calculation. This range may extend to higher resolutions if particles are smoother.

We suggest that shape-dependent drag equations should also be evaluated for modelling the transport of other non-spherical atmospheric particulates of a similar size range to volcanic ash, including desert dust (Chou et al., 2008), wildfire embers (Anthenien et al., 2006), pollen and spores (Schwendemann et al., 2007).

7. Recommendations for including ash shape in dispersion models

We present a table of default shapes to be used with shape-dependent drag equations for modelling atmospheric ash concentrations and travel distance (Table 2). The shape ranges given are based on the mean and standard deviation of ash shape (Figure 7). Bagheri and Bonadonna (2016a) give the extremes of a shape range for volcanic ash: flatness = 0.07 – 1.0 and elongation = 0.24 – 1.0. Although we do not consider the full shape ranges, minimum shape in a sample will affect the maximum travel distance of the ash particles (for a given size). In the case of very far-travelled ash, including tephra preserved as non-visible horizons in sediment sequences (cryptotephra), unusual shapes can allow grains to travel significantly further than spherical equivalents (e.g., Stevenson et al., 2015), creating a discrepancy between the measured and modelled travel distance of cryptotephra grains (Saxby et al., in press). Although extreme shapes may be relevant in considering the transport of individual grains, our recommendations based on mean shape are aimed at forecasting ash cloud location and concentration. The drag equations given all produce more accurate velocity estimates for volcanic ash particles than a spherical assumption; they are suitable for forecasting the dispersion of ash in particle size ranges typically modelled by VAACs; and our shape data are calculated from axis lengths, which are insensitive to image resolution, or surface area at resolutions we find to be effective for drag calculation. We recommend the use of these shape values as defaults in place of a spherical approximation in volcanic ash dispersion models.

References

Alfano, F., Bonadonna, C., Delmelle, P., Costantini, L., 2011. Insights on tephra settling velocity from morphological observations. Journal of Volcanology and Geothermal Research 208, 86–98.
URL http://dx.doi.org/10.1016/j.jvolgeores.2011.09.013

Anthenien, R. A., Tse, S. D., Carlos Fernandez-Pello, A., 7 2006. On the trajectories of embers initially elevated or lofted by small scale ground fire plumes in high winds. Fire Safety Journal 41 (5), 349–363.
URL https://www.sciencedirect.com/science/article/pii/S0379711206000208

Table 2: Recommended default shape descriptors to be used with shape-dependent drag equations in volcanic ash dispersion models.

Drag equation	Shape descriptor	Shape equation	Particle size fraction	Shape range
Ganser (1993)	Sphericity	Sphericity: $\psi_G = \frac{\pi^{\frac{1}{3}}(6V)^{\frac{2}{3}}}{A_{\text{surf}}}$, or sphericity of an approximate ellipsoid: $\psi_e = \frac{\pi^{\frac{1}{3}}(6V)^{\frac{2}{3}}}{A_e}$	$< 10^2$ µm	0.3 – 0.8
			10^2 µm – 10^4 µm	0.1 – 0.8
Bagheri and Bonadonna (2016b)	Elongation e and flatness f	$e = \frac{I}{L}$, $f = \frac{S}{I}$	$< 10^4$ µm	Elongation: 0.4 – 0.9 Flatness: 0.6 – 0.9
Dioguardi et al. (2018)	Dioguardi shape factor Ψ_D	$\Psi_D \approx 0.83\psi_e$ where $\psi_e = \frac{\pi^{\frac{1}{3}}(6V)^{\frac{2}{3}}}{A_e}$	$< 10^2$ µm	0.2 – 0.5
			10^2 µm – 10^4 µm	0.1 – 0.7

Arason, P., Petersen, G. N., Bjornsson, H., 2011. Observations of the altitude of the volcanic plume during the eruption of Eyjafjallajökull, April-May 2010. Earth System Science Data 3, 9–17.
URL https://www.earth-syst-sci-data.net/3/9/2011/

Bagheri, G., Bonadonna, C., 1 2016a. Aerodynamics of Volcanic Particles: Characterization of Size, Shape, and Settling Velocity. Volcanic Ash, 39–52.
URL https://www.sciencedirect.com/science/article/pii/B9780081004050000057

Bagheri, G., Bonadonna, C., 2016b. On the drag of freely falling non-spherical particles. Powder Technology 301, 526–544.
URL http://dx.doi.org/10.1016/j.powtec.2016.06.015

Bagheri, G. H., Bonadonna, C., Manzella, I., Vonlanthen, P., 2015. On the characterization of size and shape of irregular particles. Powder Technology 270, 141–153.
URL https://doi.org/10.1016/j.powtec.2014.10.015

Beckett, F. M., Witham, C. S., Hort, M. C., Stevenson, J. A., Bonadonna, C., Millington, S. C., 2015. Sensitivity of dispersion model forecasts of volcanic ash to the physical characteristics of the particles. Journal of Geophysical Research.

Buckland, H. M., Eychenne, J., Rust, A. C., Cashman, K. V., 1 2018. Relating the physical properties of volcanic rocks to the characteristics of ash generated by experimental

abrasion. Journal of Volcanology and Geothermal Research 349, 335–350.
URL https://www.sciencedirect.com/science/article/pii/S0377027317306832

Chou, C., Formenti, P., Maille, M., Ausset, P., Helas, G., Harrison, M., Osborne, S., 12 2008. Size distribution, shape, and composition of mineral dust aerosols collected during the African Monsoon Multidisciplinary Analysis Special Observation Period 0: Dust and Biomass-Burning Experiment field campaign in Niger, January 2006. Journal of Geophysical Research: Atmospheres 113 (D23).
URL https://agupubs.onlinelibrary.wiley.com/doi/full/10.1029/2008JD009897%4010.1002/%28ISSN%292169-8996.DABEX1#jgrd14744-fig-0007

Del Bello, E., Taddeucci, J., De'Michieli Vitturi, M., Scarlato, P., Andronico, D., Scollo, S., Kueppers, U., Ricci, T., 2017. Effect of particle volume fraction on the settling velocity of volcanic ash particles: Insights from joint experimental and numerical simulations. Scientific Reports 7.
URL http://dx.doi.org/10.1038/srep39620

Dellino, P., Mele, D., Bonasia, R., Braia, G., La Volpe, L., Sulpizio, R., 2005. The analysis of the influence of pumice shape on its terminal velocity. Geophysical Research Letters 32.
URL https://agupubs.onlinelibrary.wiley.com/doi/full/10.1029/2005GL023954

Dioguardi, F., Mele, D., Dellino, P., 2018. A new one-equation model of fluid drag for irregularly shaped particles valid over a wide range of Reynolds number: Aerodynamic drag of irregular particles. Journal of Geophysical Research: Solid Earth 123, 144–156.
URL https://agupubs.onlinelibrary.wiley.com/doi/10.1002/2017JB014926

Dioguardi, F., Mele, D., Dellino, P., Dürig, T., 2017. The terminal velocity of volcanic particles with shape obtained from 3D X-ray microtomography. Journal of Volcanology and Geothermal Research 329, 41–53.
URL http://dx.doi.org/10.1016/j.jvolgeores.2016.11.013

589 Dufek, J., Manga, M., 2008. In situ production of ash in pyroclastic flows. Journal of
590 Geophysical Research: Solid Earth 113.
591 URL https://agupubs.onlinelibrary.wiley.com/doi/10.1029/
592 2007JB005555

593 Dunbar, N. W., Iverson, N. A., Van Eaton, A. R., Sigl, M., Alloway, B. V., Kurbatov, A. V.,
594 Mastin, L. G., McConnell, J. R., Wilson, C. J. N., 2017. New Zealand supereruption
595 provides time marker for the Last Glacial Maximum in Antarctica. Scientific Reports
596 7 (1), 12238.
597 URL https://www.nature.com/articles/s41598-017-11758-0

598 Durant, A. J., Bonadonna, C., Horwell, C. J., 2010. Atmospheric and environmental
599 impact of volcanic particulates. Elements 6, 235–240.
600 URL https://pubs.geoscienceworld.org/msa/elements/
601 article-abstract/6/4/235/137866

602 Ersoy, O., Şen, E., Aydar, E., Tatar, I., Çelik, H. H., 2010. Surface area and volume mea-
603 surements of volcanic ash particles using micro-computed tomography (micro-CT): A
604 comparison with scanning electron microscope (SEM) stereoscopic imaging and geo-
605 metric considerations. Journal of Volcanology and Geothermal Research 196, 281–286.
606 URL https://doi.org/10.1016/j.jvolgeores.2010.08.004

607 Ganser, G. H., 1993. A rational approach to drag prediction of spherical and nonspherical
608 particles. Powder Technology 77, 143–152.
609 URL https://doi.org/10.1016/0032-5910(93)80051-B

610 Gislason, S. R., Hassenkam, T., Nedel, S., Bovet, N., Eiriksdottir, E. S., Alfredsson, H. A.,
611 Hem, C. P., Balogh, Z. I., Dideriksen, K., Oskarsson, N., Sigfusson, B., Larsen, G.,
612 Stipp, S. L. S., 2011. Characterization of Eyjafjallajökull volcanic ash particles and a
613 protocol for rapid risk assessment. Proceedings of the National Academy of Sciences
614 108 (18), 7307–7312.
615 URL https://doi.org/10.1073/pnas.1015053108

616 Higgins, M. D., Roberge, J., 8 2003. Crystal Size Distribution of Plagioclase and Amphi-
617 bole from Soufriere Hills Volcano, Montserrat: Evidence for Dynamic Crystallization-
618 Textural Coarsening Cycles. Journal of Petrology 44 (8), 1401–1411.

URL https://academic.oup.com/petrology/article-lookup/doi/10.1093/petrology/44.8.1401

Hort, M. C., 2016. VAAC operational dispersion model configuration snap shot Version 2. Tech. Rep. March, NCEP, Washington.
URL https://www.wmo.int/aemp/VAAC-BP-2016

Horwell, C. J., Stannett, G. W., Andronico, D., Bertagnini, A., Fenoglio, I., Fubini, B., Le Blond, J. S., Williamson, B. J., 2010. A physico-chemical assessment of the health hazard of Mt. Vesuvius volcanic ash. Journal of Volcanology and Geothermal Research 191, 222–232.
URL http://dx.doi.org/10.1016/j.jvolgeores.2010.01.014

Jorry, S. J., Hasler, C.-A., Davaud, E., 5 2006. Hydrodynamic behaviour of Nummulites: implications for depositional models. Facies 52 (2), 221–235.
URL http://link.springer.com/10.1007/s10347-005-0035-z

Komar, P. D., Reimers, C. E., 3 1978. Grain Shape Effects on Settling Rates. The Journal of Geology 86 (2), 193–209.
URL https://www.journals.uchicago.edu/doi/10.1086/649674

Koyaguchi, T., Ohno, M., 4 2001. Reconstruction of eruption column dynamics on the basis of grain size of tephra fall deposits: 2. Application to the Pinatubo 1991 eruption. Journal of Geophysical Research: Solid Earth 106 (B4), 6513–6533.
URL http://doi.wiley.com/10.1029/2000JB900427

Larsen, G., Dugmore, A., Newton, A., 1999. The Holocene Geochemistry of historical-age silicic tephras in Iceland. The Holocene 9 (4), 463–471.
URL https://doi.org/10.1191/095968399669624108

Larsen, G., Newton, A. J., Dugmore, A. J., Vilmundardóttir, E. G., 2001. Geochemistry, dispersal, volumes and chronology of Holocene silicic tephra layers from the Katla volcanic system, Iceland. Journal of Quaternary Science 16 (2), 119–132.
URL https://doi.org/10.1002/jqs.587

Liu, E. J., Cashman, K. V., Rust, A. C., 2015. Optimising shape analysis to quantify volcanic ash morphology. GeoResJ 8, 14–30.

URL http://dx.doi.org/10.1016/j.grj.2015.09.001

Liu, E. J., Cashman, K. V., Rust, A. C., Höskuldsson, A., 2017. Contrasting mechanisms of magma fragmentation during coeval magmatic and hydromagmatic activity: the Hverfjall Fires fissure eruption, Iceland. Bulletin of Volcanology 79 (10).
URL https://doi.org/10.1007/s00445-017-1150-8

Liu, E. J., Oliva, M., Antoniades, D., Giralt, S., Granados, I., Pla-Rabes, S., Toro, M., Geyer, A., 2016. Expanding the tephrostratigraphical framework for the South Shetland Islands, Antarctica, by combining compositional and textural tephra characterisation. Sedimentary Geology 340, 49–61.
URL http://dx.doi.org/10.1016/j.sedgeo.2015.08.002

Mangerud, J., Lie, S. E., Furnes, H., Kristiansen, I. L., Lømo, L., 1984. A Younger Dryas ash bed in western Norway, and its possible correlations with tephra in cores from the Norwegian Sea and the North Atlantic. Quaternary Research 21, 85–104.
URL https://doi.org/10.1016/0033-5894(84)90092-9

Mele, D., Dellino, P., Sulpizio, R., Braia, G., 2011. A systematic investigation on the aerodynamics of ash particles. Journal of Volcanology and Geothermal Research 203, 1–11.
URL http://dx.doi.org/10.1016/j.jvolgeores.2011.04.004

Mele, D., Dioguardi, F., 2018. The grain size dependency of vesicular particle shapes strongly affects the drag of particles. First results from microtomography investigations of Campi Flegrei fallout deposits. Journal of Volcanology and Geothermal Research 353, 18–24.
URL https://doi.org/10.1016/j.jvolgeores.2018.01.023

Oakey, R. J., Green, M., Carling, P. A., Lee, M. W., Sear, D. A., Warburton, J., 11 2005. Grain-Shape Analysis–A New Method for Determining Representative Particle Shapes for Populations of Natural Grains. Journal of Sedimentary Research 75 (6), 1065–1073.
URL https://pubs.geoscienceworld.org/jsedres/article/75/6/1065-1073/144996

Riley, C. M., Rose, W. I., Bluth, G. J. S., 2003. Quantitative shape measurements of distal volcanic ash. Journal of Geophysical Research: Solid Earth 108 (B10), 1–15.

URL http://doi.wiley.com/10.1029/2001JB000818

Rolph, G., Ngan, F., Draxler, R., 10 2014. Modeling the fallout from stabilized nuclear clouds using the HYSPLIT atmospheric dispersion model. Journal of Environmental Radioactivity 136, 41–55.
URL https://www.sciencedirect.com/science/article/pii/S0265931X14001453

Rose, W. I., Chesner, C. A., 1987. Dispersal of ash in the great Toba eruption, 75 ka. Geology 15, 913–917.

Rose, W. I., Durant, A. J., 2009. Fine ash content of explosive eruptions. Journal of Volcanology and Geothermal Research 186, 32–39.
URL http://dx.doi.org/10.1016/j.jvolgeores.2009.01.010

Rust, A. C., Cashman, K. V., 2011. Permeability controls on expansion and size distributions of pyroclasts. Journal of Geophysical Research 116.
URL https://doi.org/10.1029/2011JB008494

Saxby, J., Beckett, F., Cashman, K., Rust, A., Tennant, E., 2018. The impact of particle shape on fall velocity: Implications for volcanic ash dispersion modelling. Journal of Volcanology and Geothermal Research 362.
URL https://doi.org/10.1016/j.jvolgeores.2018.08.006

Saxby, J., Cashman, K. V., Rust, A. C., Beckett, F. M., in press. The importance of grain size and shape in controlling the dispersion of the Vedde cryptotephra. Journal of Quaternary Science (Special Issue: INTAV Tephra).
URL https://doi.org/10.1002/jqs.3152

Schwendemann, A. B., Wang, G., Mertz, M. L., McWilliams, R. T., Thatcher, S. L., Osborn, J. M., 8 2007. Aerodynamics of saccate pollen and its implications for wind pollination. American Journal of Botany 94 (8), 1371–1381.
URL http://www.ncbi.nlm.nih.gov/pubmed/21636505http://doi.wiley.com/10.3732/ajb.94.8.1371

Scollo, S., Folch, A., Costa, A., 2008. A parametric and comparative study of different tephra fallout models. Journal of Volcanology and Geothermal Research 176 (2), 199–

211.
URL https://doi.org/10.1016/j.jvolgeores.2008.04.002

Speijer, R. P., Van Loo, D., Masschaele, B., Vlassenbroeck, J., Cnudde, V., Jacobs, P., 8 2008. Quantifying foraminiferal growth with high-resolution X-ray computed tomography: New opportunities in foraminiferal ontogeny, phylogeny, and paleoceanographic applications. Geosphere 4 (4), 760.
URL https://pubs.geoscienceworld.org/geosphere/article/4/4/760-763/31235

Stevenson, J. A., Millington, S. C., Beckett, F. M., Swindles, G. T., Thordarson, T., 2015. Big grains go far: Understanding the discrepancy between tephrochronology and satellite infrared measurements of volcanic ash. Atmospheric Measurement Techniques 8 (5), 2069–2091.

Vonlanthen, P., Rausch, J., Ketcham, R. A., Putlitz, B., Baumgartner, L. P., Grobéty, B., 2015. High-resolution 3D analyses of the shape and internal constituents of small volcanic ash particles: The contribution of SEM micro-computed tomography (SEM micro-CT). Journal of Volcanology and Geothermal Research 293, 1–12.
URL http://dx.doi.org/10.1016/j.jvolgeores.2014.11.016

Wastegård, S., Björck, S., Possnert, G., Wohlfarth, B., 1998. Evidence for the occurrence of Vedde Ash in Sweden: radiocarbon and calendar age estimates. Journal of Quaternary Science 13 (3), 271–274.
URL https://doi.org/10.1002/(SICI)1099-1417(199805/06)13:3%3C271::AID-JQS372%3E3.0.CO;2-4

Westbrook, C. D., Sephton, E. K., 2017. Using 3-D-printed analogues to investigate the fall speeds and orientations of complex ice particles. Geophysical Research Letters 44 (15), 7994–8001.
URL https://doi.org/10.1002/2017GL074130

White, F. M., 1974. Viscous Fluid Flow. McGraw-Hill, New York.

Wilson, L., Huang, T. C., 1979. The influence of shape on the atmospheric settling velocity of volcanic ash particles. Earth and Planetary Science Letters 44 (2), 311–324.
URL https://doi.org/10.1016/0012-821X(79)90179-1